JGR Atmospheres

RESEARCH ARTICLE
10.1029/2021JD035806

Key Points:

- A new method is introduced to quantify the strength of Kelvin circulation response to the Madden-Julian Oscillation (MJO) with varying zonal scales
- The MJO is most likely to continue its propagation when both zonal wind and geopotential signals of the Kelvin circulation are present
- Meridional moisture advection is most important in supporting MJO eastward propagation

Correspondence to:
A. H. Berrington,
andrew.berrington@ou.edu

Citation:
Berrington, A. H., Sakaeda, N., Dias, J., & Kiladis, G. N. (2022). Relationships between the eastward propagation of the Madden-Julian Oscillation and its circulation structure. *Journal of Geophysical Research: Atmospheres*, *127*, e2021JD035806. https://doi.org/10.1029/2021JD035806

Received 7 SEP 2021
Accepted 9 AUG 2022

Relationships Between the Eastward Propagation of the Madden-Julian Oscillation and Its Circulation Structure

Andrew H. Berrington[1], Naoko Sakaeda[1], Juliana Dias[2], and George N. Kiladis[2]

[1]School of Meteorology, University of Oklahoma, Norman, OK, USA, [2]National Oceanic and Atmospheric Administration, Physical Sciences Laboratory, Boulder, CO, USA

Abstract The circulation associated with convection of the Madden-Julian Oscillation (MJO) has been suggested to have an impact on its propagation by a number of previous studies. This circulation contains both flanking Rossby waves to the rear and a Kelvin wave leading the convective center. In this study, individual MJO convective envelopes from a 40-year database are tracked, a technique to scale the MJO by its zonal wavelength is employed, and statistical methods are used to assess how the MJO circulation pattern might impact its eastward propagation downstream. Results suggest that continuous eastward propagation of the MJO is favored when a strong Kelvin wave circulation is present east of MJO convection, indicated by both an easterly zonal wind anomaly and negative geopotential height anomaly. In addition to the known significance of having Kelvin wave easterly wind anomalies, the results of this study highlight that the existence of negative geopotential height is important to supporting moistening and MJO propagation. It is found that importance of the Kelvin wave signal to MJO propagation depends on the region that the MJO is located over. Kelvin wave circulation east of MJO convection enhances moistening to support continuous eastward propagation of the MJO, mainly through meridional moisture advection due to the coupling between the Kelvin wave and Rossby-like disturbances east of the active convection. The roles of boundary layer convergence and vertical moistening are also discussed.

1. Introduction

As the dominant mode of intraseasonal variability in the tropics, the Madden-Julian Oscillation (MJO), first identified in Madden and Julian (1971), represents a vital connection between weather and climate timescales. The MJO is a planetary-scale, organized region of anomalous convection and associated circulation that propagates eastward at speeds of roughly 5 m s^{-1} (Madden & Julian, 1994; M. C. Wheeler & Hendon, 2004; Kiladis et al., 2005; Zhang, 2005). Despite the global impacts of the MJO on a broad range of tropical and extratropical weather and climate (Barrett & Leslie, 2009; Bessafi & Wheeler, 2006; Henderson et al., 2016; Klotzbach, 2010; Maloney & Hartmann, 2000; Pai et al., 2011; Yoo et al., 2012), the current operational and global circulation models (GCMs) struggle to capture the fundamental characteristics of the MJO (B. Wang & Lee, 2017; Hamill & Kiladis, 2014; Jiang et al., 2020; Vitart & Molteni, 2010). The objective of this study is to improve our understanding of the mechanisms that control the eastward propagation of the moisture and precipitation anomalies associated with the MJO, which is a crucial step toward predicting its evolution.

Current forecast systems often do not capture MJO propagation speed well (Hamill & Kiladis, 2014; Vitart & Molteni, 2010), a model deficiency that can have a substantial effect on medium and extended range prediction across the globe (Ferranti et al., 1990; Gottschalck et al., 2013; H. M. Kim et al., 2014). Two related processes that have been suggested to drive eastward propagation of the moisture and rainfall anomalies associated with the MJO are (a) boundary layer convergence and (b) meridional advection of moisture. These processes occur through interactions between moisture and MJO circulation, where the latter is qualitatively consistent with a coupled Kelvin-Rossby wave response to a tropical heating source (B. Wang & Lee, 2017; Gill, 1980; Hendon & Salby, 1994; Kiladis et al., 2005). To the east of MJO enhanced convection, anomalous low pressure and easterly winds appear around the equatorial lower-troposphere in the form of a Kelvin wave, accompanied by boundary layer moisture convergence. Therefore, the existence and strength of a Kelvin wave circulation is considered important for deepening of the moist boundary layer (Johnson & Ciesielski, 2017; Kemball-Cook & Weare, 2001) and a build-up of convective instability (Hsu & Li, 2012). A pair of anticyclonic equatorial Rossby waves also exists in the lower troposphere to the west of MJO suppressed convection (east of enhanced convection), as highlighted by D. Kim et al. (2014), Feng et al. (2015), and DeMott et al. (2018). The poleward

flow associated with these Rossby waves is thought to moisten the column through meridional advection of background moisture, supporting eastward propagation of MJO convection.

B. Wang and Lee (2017) also showed that only a small fraction of GCMs had reliable skill in forecasting MJO propagation from the Indian Ocean into the West Pacific. A major difficulty in forecasting the MJO is related to propagation of the precipitation and moisture anomalies across the Maritime Continent (Fu et al., 2013; H. M. Kim et al., 2016; Jiang et al., 2020; Vitart & Molteni, 2010; Weaver et al., 2011), where models commonly depict MJO decay to a greater extent than is actually observed (D. Kim et al., 2009; Kerns & Chen, 2016; Zhang & Ling, 2017). Here, complex terrain affects the circulation of the MJO, the diurnal cycle of its convection, and surface fluxes (Ahn et al., 2020; DeMott et al., 2018; Ling et al., 2019) and results in changes in the propagation characteristics (B. Wang et al., 2019; Zhang & Ling, 2017), where some events continue into the West Pacific, while others weaken.

Several studies have found differing processes driving or impeding MJO propagation beyond the Maritime Continent. D. Kim et al. (2014) found that the existence of a suppressed convective envelope ahead of the MJO enhanced convective envelope is important for the MJO to continue propagating. A Rossby wave response to the negative heating anomaly associated with the convectively suppressed region drives poleward, meridional wind anomalies that lead to anomalous, off-equatorial, lower tropospheric moistening eastward of MJO enhanced convection, which is not present in the non-propagating cases. Chen and Wang (2018) also determined that a leading suppressed convective region was a strong precursor signal for propagation. The suppressed convective region itself was a result of either a preceding MJO-related dry phase propagating eastward into the West Pacific, or a two-way interaction between preceding Indian Ocean suppressed convection and a tropical-extratropical teleconnection that generates a western North Pacific cyclonic circulation in the upper levels. The western North Pacific extratropical cyclone induces upper level convergence over the western tropical Pacific and thereby strengthens the suppressed convective region. This increased magnitude of the suppressed convective region leads to stronger boundary layer convergence eastward of the enhanced convective center, triggering new convection and supporting MJO eastward propagation.

Meanwhile, Feng et al. (2015) found that westward-propagating Rossby waves in the equatorial Pacific, independent of the MJO, lead to dry air intrusions ahead of the convectively active region, which then hinders convective development eastward downstream of the convective center and halts propagation. Meridional advection of background mean moist static energy was not significantly affected by the strength of the leading convectively suppressed region, contrasting with D. Kim et al. (2014). Findings from DeMott et al. (2018) suggest a similar mechanism for MJO decay over the Maritime Continent in some cases. Feng et al. (2015) also determined a dichotomy of moistening processes in the propagating cases. They found the MJO can propagate across the Maritime Continent without a strong suppressed region leading the convective center, when anomalous vertical moisture advection sustained column moisture.

These studies suggest that the key elements to propagation of MJO rainfall and moisture anomalies are moistening processes associated with the Rossby-Kelvin wave circulation of the MJO. However, they do not agree on what is the dominant moistening process, diverging amongst the horizontal advection, mid-tropospheric vertical advection, and shallow moistening through boundary layer convergence. The diversity of MJO propagation was further tested by B. Wang et al. (2019), who postulated that the primary mechanism in establishing propagation across the Maritime Continent of MJO events centered in the eastern Indian Ocean is the strength of the Kelvin wave response driving frictional boundary layer moisture convergence ahead of the convective center. Speed of propagation is also influenced by the Kelvin response's strength and zonal extent, with faster propagation occurring with a higher amplitude and longer Kelvin response (Chen & Wang, 2020). Jiang et al. (2015) found that correctly simulating the Kelvin wave component in a set of GCMs was crucial in establishing prediction skill of the MJO's propagation, while adequately depicting the mean moisture field is also crucial (Gonzalez & Jiang, 2017).

Motivated by the conflicting results of previous studies on the dynamics of MJO propagation across the Maritime Continent, this study seeks to re-examine the role of Kelvin-Rossby circulation on MJO propagation. To achieve this objective, this study addresses the two questions below.

1. Does MJO circulation structure have significant relationships with the MJO crossing the Maritime Continent?

2. What are the mechanisms relating MJO circulation and the eastward propagation of its convection across the MC?

We introduce a new method to quantify the lower-tropospheric Kelvin-Rossby circulation strength to examine its effects on MJO propagation. Subsequently, we use moisture budget analysis to understand the physical processes through which the circulation influences moisture evolution and MJO propagation.

2. Data and Methods

2.1. Data

To track latitude and longitude progression of the convectively enhanced phase of the MJO, we use NOAA Interpolated Daily OLR (Liebmann & Smith, 1996) on a 2.5° by 2.5° horizontal grid and during the period of 1979–2018. For atmospheric variables, we use 6 hourly, 2.5° ERA-Interim (Dee et al., 2011) fields averaged daily. The OLR is filtered for the MJO using the M. Wheeler and Kiladis (1999) method retaining intraseasonal periods of 20–100 days and eastward zonal wavenumbers 1–10, following the removal of the mean and the first three harmonics of the seasonal cycle. Unless otherwise specified, wind and geopotential height are filtered for 20–100 day periods, and zonal wavenumbers higher than 10 are removed to reduce noise. We include westward zonal wavenumbers for these variables to capture the circulation associated with the MJO that may not necessarily propagate at the same speed as its convective envelope (D. Kim et al., 2014; DeMott et al., 2018; Feng et al., 2015). This study only examines MJO events that occur during the period from November to March because the Boreal Summer Intraseasonal Oscillation exhibits significantly different characteristics compared to its boreal winter counterpart (B. Wang & Xie, 1997; Lawrence & Webster, 2002; Lee et al., 2013).

2.2. Tracking Algorithm

We use the MJO-filtered OLR anomalies to identify and track MJO convective envelopes in time, longitude, and latitude, through an algorithm that extends from Kerns and Chen (2016) and Dias et al. (2017). The algorithm operates as follows:

1. On each day, contiguous regions of MJO-filtered OLR anomaly above or below its upper and lower fifteenth percentile values within the full longitude band of 15°S–15°N are identified as convectively suppressed and enhanced envelopes of the MJO, respectively. The fifteenth percentile (about $\pm 10\ Wm^{-2}$) is close to the daily standard deviation of MJO-filtered OLR over the Indo-Pacific basin (Kiladis et al., 2005). We will refer to them as MJO "convective envelopes".
2. If a convective envelope overlaps horizontally with another envelope in the next day, it is considered the same convective envelope and its propagation is tracked as an "event". This step is less restrictive than the method of Kerns and Chen (2016), where the convective envelope has to overlap for at least 50%. However, we determined that such a restriction is not necessary for filtered OLR anomalies and our method allows us to better capture MJO events that are known to appear as if they "jumped" across the Maritime Continent due to typical weakening over the Maritime Continent (B. Wang et al., 2019).
3. When a single convective envelope splits into two separate objects in the subsequent time-step, the objects that overlaps more in horizontal space with the original convective envelope is maintained as the same event, while the convective envelope with less horizontal overlap initiates a new event in the tracking algorithm. When two envelopes merge into a single convective envelope in the subsequent time-step, the convective envelope that had a larger horizontal overlap with the merged convective envelope is maintained as the same event, while the other with less horizontal overlap is terminated by the algorithm.
4. Latitude and longitude centroids of the convective envelopes are computed using the absolute values of the filtered negative OLR anomalies. The convective envelopes are terminated when their centroid moves poleward of the 15°S–15°N latitude band.

Among all the identified events, we only analyze those that last more than 5 days. We also only include events that have passed through or initiated over the Indian Ocean (45°–95°E) to examine factors that influence MJO propagation across the Maritime Continent. A total of 240 events are identified using this criteria, or roughly six events per season over the 40 year database.

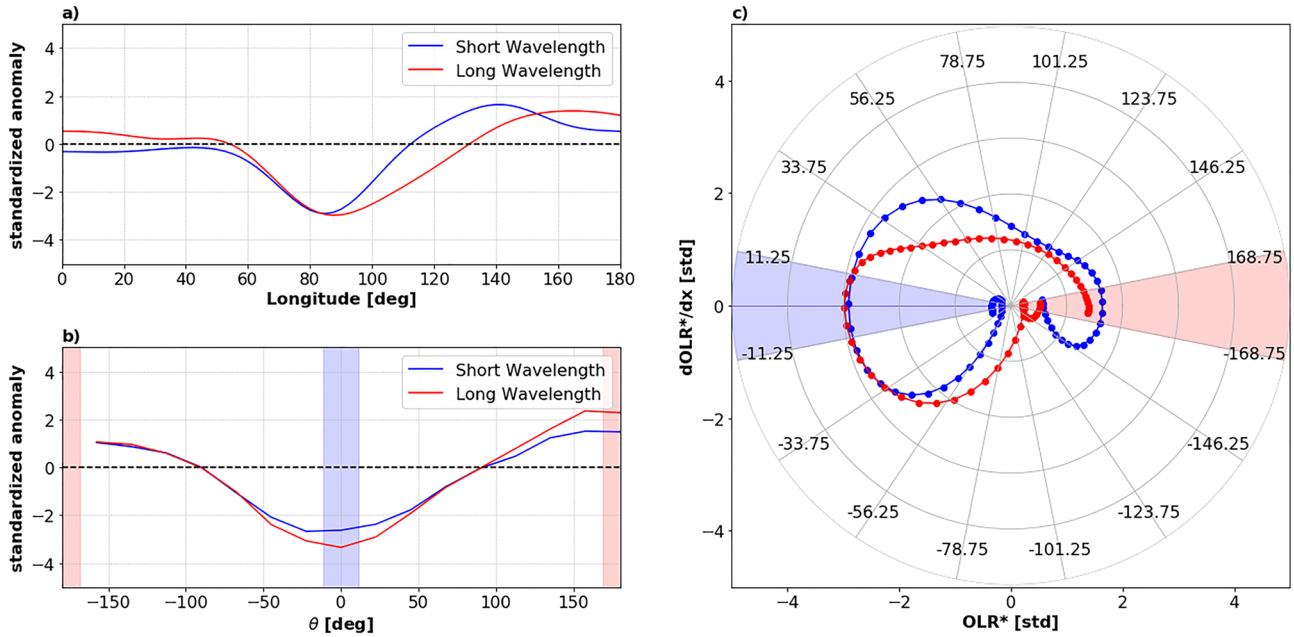

Figure 1. An example of composite *OLR** averaged 5° south to north of the latitude centroid for five short wavelength (blue lines) and five long wavelength events (red lines) within 80−100°E plotted via (a) standard longitude coordinates and (b) theta coordinates. (c) A zonal phase diagram of the same event defined by *OLR** and its zonal gradient. For (c), the data plotted is in longitude coordinates. Red and blue shaded regions in (b and c) represent the regions of suppressed convection and active convection, respectively.

2.3. Circulation Indices

Previous studies assessing the spatial characteristics of the MJO—through both horizontal mapping and vertical cross-sections—have often computed composites of MJO signals in standard latitude-longitude coordinates (Adames & Wallace, 2015; B. Wang et al., 2019; Feng et al., 2015; H. M. Kim et al., 2016; Kiladis et al., 2005). Since MJO convection appears with a range of zonal wavenumbers, individual events may contain different zonal scales. We may also assume that the zonal extent of MJO circulation scales with the zonal extent of the convection itself, as suggested by B. Wang et al. (2019) and Chen and Wang (2020). In this case, a quantification of Kelvin and Rossby circulation of the MJO should also be done according to the zonal scale of MJO convection. We scale individual events by the zonal extents of MJO convection through a coordinate transformation. This is completed prior to calculating composite means or other analysis. To do this, we define a "zonal phase" angle θ as

$$\theta = \tan^{1}\left(\frac{OLR^{*}}{\left[\frac{dOLR}{dx}\right]^{*}}\right) \quad (1)$$

where *OLR** represents the standardized anomaly of MJO-filtered OLR, averaged from 5° north to south of the latitude centroid of the MJO convective envelope, and $\left[\frac{dOLR}{dx}\right]^{*}$ is the standardized anomaly of the zonal gradient of the *OLR** calculated across the full longitude domain from 0° to 360°, before any coordinate transformation occurs. Both the OLR anomaly and its zonal gradient are standardized using their climatological standard deviations between 15°S and 15°N prior to calculation. Similar methods were undertaken in Riley et al. (2011) and Sakaeda et al. (2020) in the time dimension.

Figures 1a–1c illustrate this transformation using a composite MJO of shorter wavelength and longer wavelength events (of comparable peak amplitudes), where Figure 1a represents the *OLR** in longitude coordinates that is averaged from 5° south to north of its latitude centroid. Figure 1c depicts how these MJO convective envelopes appear on a phase diagram defined by *OLR** and its zonal gradient. Variables at longitudes that correspond to each bin are averaged and area-weighted to transform data from longitude to zonal phase (theta) coordinates.

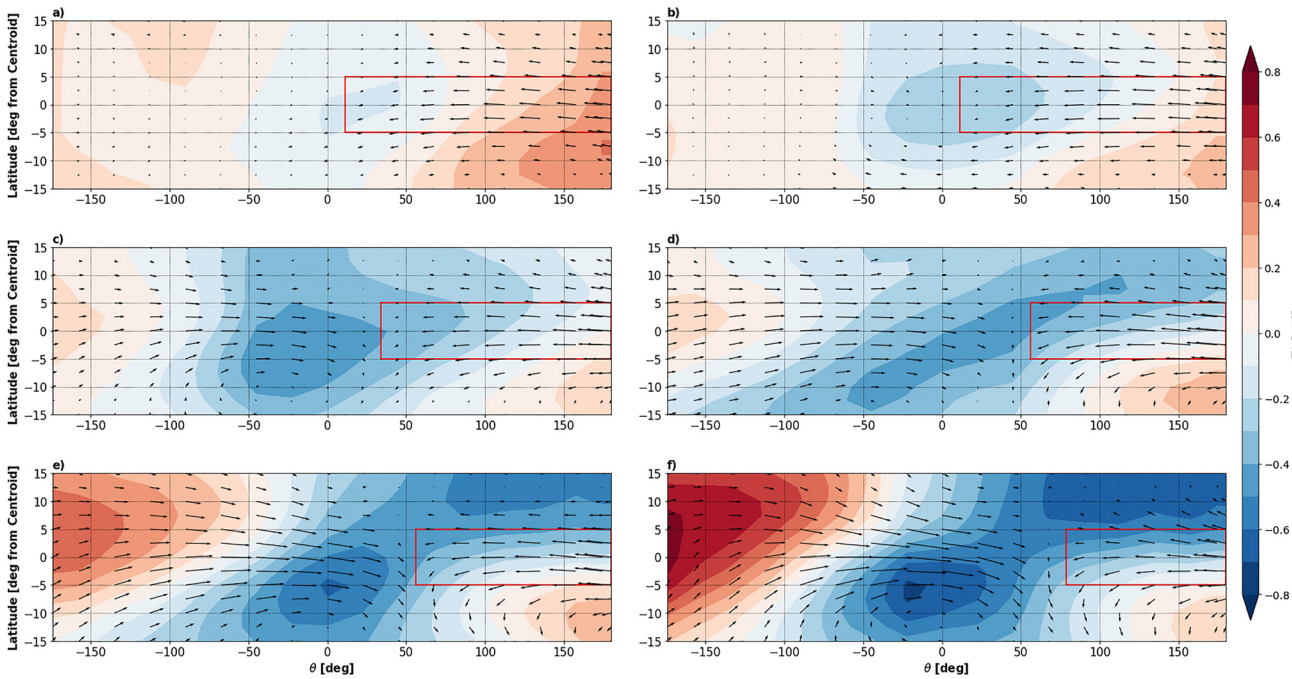

Figure 2. Composite mean 850 hPa Z^* (color-shading, in std) and V_H' (vectors, in m s^{-1}) in theta-latitude coordinates for (a) all cases centered between 40 and 60°E, (b) all cases centered between 60 and 80°E, (c) all cases centered between 80 and 100°E, (d) all cases centered between 100 and 120°E, (e) all cases centered between 120 and 140°E, and (f) all cases centered between 140 and 160°E. Red boxes indicate the regions used to create the zonal wind and geopotential height indices for each longitude range.

Figure 1b represents the *OLR** of the event (Figure 1a) in the transformed theta coordinates. The zonal phase angle represents the relative location with respect to the location of the MJO convective center, where −180° is the positive *OLR** maximum to the west of the convective center, 0° is the negative *OLR** at the convective center, and +180° is the positive *OLR** maximum to the east of the convective center. This process normalizes the scale of the *OLR** by its own zonal wavelength.

We quantify the strength of Kelvin-Rossby circulation using filtered 850 hPa zonal wind and geopotential height, after transforming their longitudes to theta coordinates, thereby using the *OLR** transformation as a guide for each event. While prior studies have often used a fixed box to quantify the circulation signal (B. Wang et al., 2019; Hsu & Li, 2012; L. Wang et al., 2018), using a fixed box does not accurately identify the signal of MJO events that do not match the zonal scale that is prescribed by the fixed box. The coordinate transformation allows us to better quantify the circulation signal for all zonal scales of MJO events. The circulation signal of MJO events is quantified separately for six 20-degree longitude bins from 40°E (western Indian Ocean) through 160°E (western Pacific). The wind and geopotential height anomalies on theta coordinates are averaged among the time steps that the centroid of an MJO event was within each longitude bin. Figure 2 shows the composite 850 hPa standardized geopotential height anomalies (Z^*) and anomalous horizontal wind on coordinates defined by theta and latitude relative to convective center for all events when their centroids are within each 20-degree longitude bin. For circulation variables that are standardized, the anomalies are calculated using the standard deviation at each grid point before transformation to theta coordinates. Figure 2 demonstrates that the circulation structure of the MJO changes as it moves eastward; therefore, the method of quantifying its circulation will also adjust accordingly.

For each MJO convective envelope at each time step, we first average the standardized zonal wind and geopotential height anomalies (U^*, Z^*) in theta coordinates averaged from 5° north to south of the latitude centroid of MJO convection. We further smooth these circulation anomalies using a Gaussian filter with a standard deviation of 5° to attenuate smaller scale noise. To measure the strength of Kelvin circulation eastward of MJO convection, we average this smoothed U^* and Z^* within the boxes shown in Figure 2 to create circulation indices. The averaging boxes are defined based on the location of low level easterlies at each longitude range. Using these circulation indices, we bin MJO events with (a) westerly ($U^* \geq 0.5$), (b) easterly ($U^* \leq -0.5$), and (c) neutral

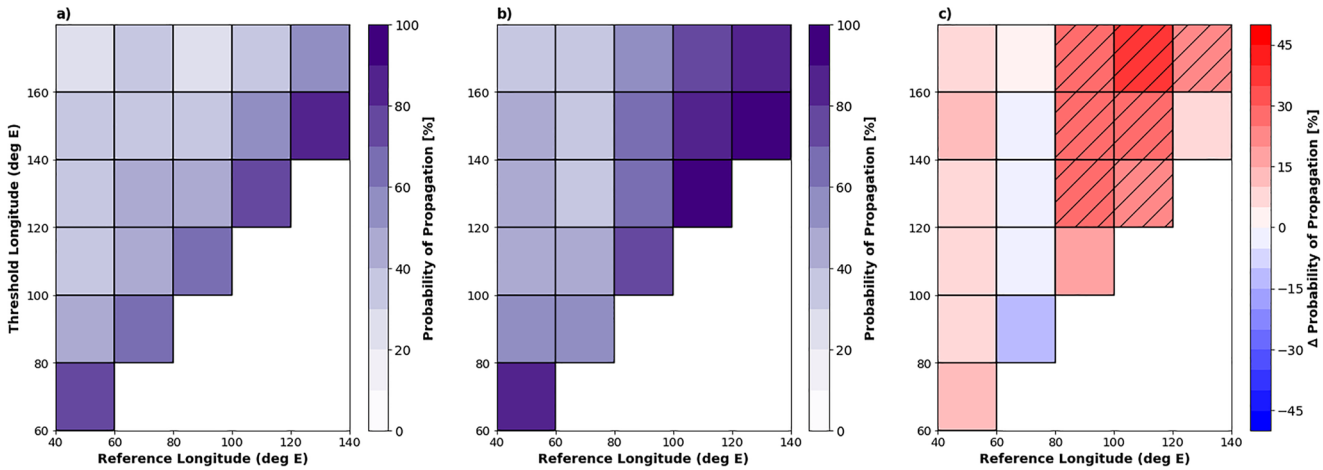

Figure 3. (a) Probabilities of propagation beyond the threshold longitudes given a positive or neutral U^* state east of the convective center at the reference longitude range, (b) as in (a), but for negative U^* state, (c) probability difference between the two U^* states. Hatching indicates significance at the 95% confidence level.

($|U^*| < 0.5$) zonal wind anomalies east of their convective centers. We group positive and neutral cases together due to small sample sizes for the positive cases and because we aim to compare MJO events with Kelvin signals (easterlies) versus those that do not. We recognize that the zonal wind alone may not accurately identify Kelvin waves, therefore we will also use the sign of the geopotential height anomaly to examine the role of Kelvin wave signal on MJO propagation.

3. Effects of MJO Circulation on Its Propagation Probabilities

Previous studies have emphasized the importance of lower tropospheric easterly wind anomalies to the east of the convective center (Adames & Wallace, 2015; B. Wang et al., 2019; Hsu & Li, 2012). The easterly anomalies associated with the Kelvin wave can moisten the environment east of the MJO through frictional boundary layer moisture convergence, surface fluxes, and horizontal moisture advection, leading to the eastward propagation of the MJO. Therefore, we will assess the effects of Kelvin wave circulation on the probabilities of MJO propagation across the Maritime Continent.

Figures 3a and 3b shows the probability that an event propagates beyond the threshold longitudes, given non-easterly (neutral or positive U^*) and easterly (negative U^*) zonal wind anomalies east of the convective center when the MJO is located within the reference longitude range. The probability of propagation is defined as the percentage of events with a given circulation pattern at a reference longitude that propagate beyond a threshold longitude. For example, the shading of the left-most column in Figure 3b shows the probability that the MJO propagates eastward beyond 60°E, 80°E, 100°E, and so forth when an event contains an easterly Kelvin component at 40–60°E. The probability of MJO propagation across the Maritime Continent is about 40%–60% depending on the reference longitudes, which is consistent with the probabilities found in prior studies (B. Wang et al., 2019; Feng et al., 2015).

Figure 3c shows the difference in the likelihood of propagation between those that do and do not contain a stronger easterly wind anomaly, where positive differences indicates that the events with easterlies have higher probability of propagation. For the reference longitude ranges of 40–60°E and 60–80°E (west to central Indian basin), we see relatively small differences in probability of propagation for all threshold longitudes. However, when the convective centers are located between 80 and 100°E and 100–120°E (eastern Indian basin to western Maritime Continent), we see higher odds of propagation for events with stronger easterly wind anomalies, with statistical significance using a Monte-Carlo test with 5,000 repetitions at the 95% confidence level.

These results indicate that when MJO convection is near or over the Maritime Continent, the presence of easterly wind anomalies to its east enhance the probability of further MJO eastward propagation. While the differences in propagation probabilities at other reference longitudes indicate a higher probability of propagation for events starting out with a stronger easterly anomaly versus weaker (except at 60–80°E), there is no statistical

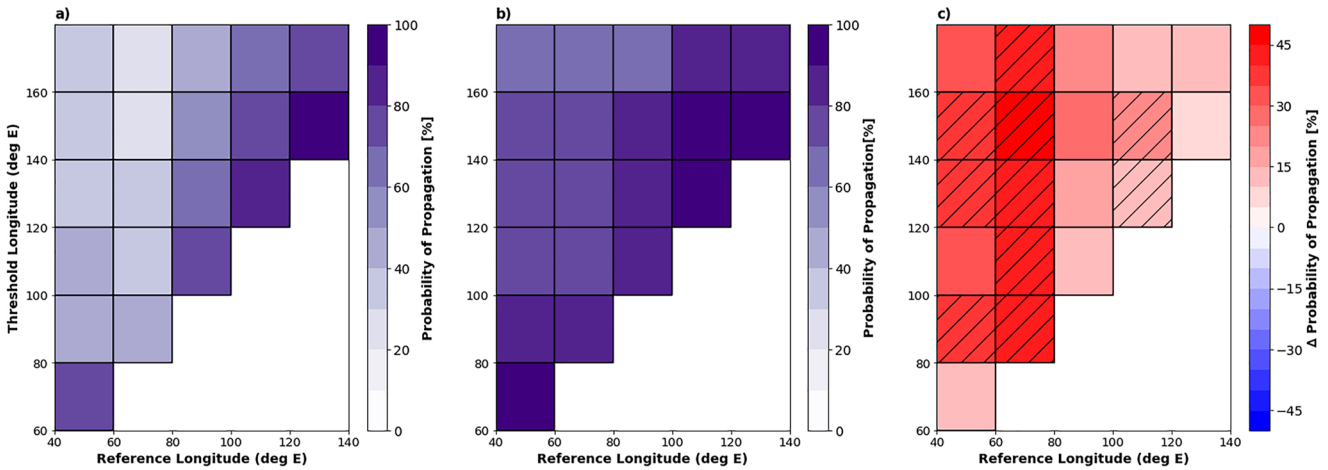

Figure 4. As in Figure 3, but instead for cases with negative *U** and differing *Z** states east of the transition.

significance indicated by the Monte-Carlo test. Although it is not shown here, we found statistically significant positive differences when MJO events with easterly anomalies were compared with events with westerlies (i.e., not including neutral cases). These results indicate that MJO events containing a stronger easterly wind anomaly east of the convective center generally propagate further than the events with weaker easterly or westerly winds. This is consistent with the results of Hsu and Li (2012) and B. Wang et al. (2019), which found that events that successfully propagated through the Maritime Continent contained stronger easterly wind anomalies ahead of the convective center.

The existence of easterlies ahead of the convective center alone does not strictly indicate the presence of Kelvin wave. However, the combination of easterly and negative geopotential height anomalies is a clear indication of the presence of a Kelvin wave as opposed to a Rossby wave (Matsuno, 1966). Therefore, we also test a combination of the two circulation indices (*U** and *Z**) east of the MJO enhanced convection. Figures 4a and 4b show the propagation probabilities of MJO events with easterlies ahead of the convective center, separated into events with non-negative (neutral or positive) and negative geopotential height anomalies (*Z**). The easterlies with negative geopotential height indicate the presence of strong Kelvin wave signal, while the easterlies with non-negative geopotential height indicate weak Kelvin wave or anti-cyclonic Rossby waves. We analyze these particular combinations to see the potential role of different wave signals to MJO propagation given the presence of easterlies ahead of its convective center.

The highest probabilities of propagation exist when the MJO event in question contains both negative *Z** and easterlies east of the convection, with values in excess of 70% through most of the events (Figure 4b). The largest positive and significant differences are for the 40–60°E and 60–80°E reference ranges. This result shows that the presence of Kelvin wave circulation east of MJO convection as indicated by both easterlies and negative geopotential height anomalies leads to the highest propagation probability. The result suggests that the presence of negative geopotential height anomalies further enhances moistening processes east of MJO convection, which will be investigated below.

Another interesting question is whether the strength of zonal wind or geopotential height anomalies influences the amplitude of MJO convection, which could influence the probabilities of continuous eastward propagation. We found that stronger MJO convection measured by *OLR** is weakly associated with stronger easterlies (*U**) or more negative geopotential height (*Z**) east of convection (not shown). However, no significant correlations were found, with exception at 120–140°E. Therefore, while some indication of stronger MJO convection resulting in a well-developed Kelvin circulation exists, there also exists a large amount of propagation variability that the circulation can explain, which is independent from the strength of MJO convection.

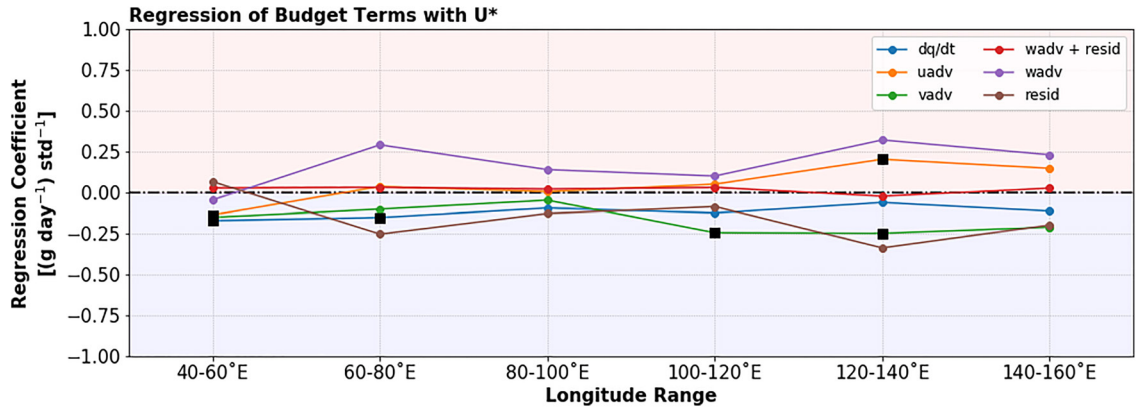

Figure 5. Regression coefficients of U^* east of the convective center versus the column-integrated moisture budget terms (g day^{-1}) averaged over the same region of theta (according to the longitude range) and over ±15° latitude from the convective center. Black square markers indicate statistical significance of the regressions at the 95% confidence level.

4. Analysis of Contributing Processes Through Moisture Budgets

In order to assess the impacts of circulation on moisture, we will use the respective states of U^* and Z^* east of the convective center to separate circulation characteristics, and we evaluate the amount of moisture near the convective center and moistening ahead (east) of convection. Intraseasonal specific humidity anomalies (q') are calculated from ERA-Interim reanalysis through the same filtering method used for the wind and geopotential height anomalies. Three-dimensional moisture budget analysis of the filtered data is performed to assess processes that contribute to moisture variability associated with MJO events. The corresponding budget terms are calculated following the methods of Yanai et al. (1973) and Adames and Wallace (2015) as

$$\frac{\partial q'}{\partial t} = -\left(u\frac{\partial q}{\partial x}\right)' - \left(v\frac{\partial q}{\partial y}\right)' - \left(\omega\frac{\partial q}{\partial p}\right)' + \frac{Q_2'}{L_v} \tag{2}$$

where q is the specific humidity, u is the zonal wind, v is the meridional wind, ω is the vertical velocity in pressure coordinates, Q_2 is the apparent moisture source (Yanai et al., 1973), and L_v is the latent heat of vapourization. Prime notation indicates MJO-filtered quantities (non-standardized). The left-hand side represents the local time rate of change in specific humidity and the right-hand side terms are as follows from left to right: zonal moisture advection, meridional moisture advection, vertical moisture advection, and the apparent moisture source (Yanai et al., 1973), which represents fluxes generated by unresolved eddies, condensation, and evaporation (Yanai & Johnson, 1993). As ERA-Interim representation of diabatic processes may be inaccurate (Kiranmayi & Maloney, 2011), we calculate the apparent moisture source as a residual to the remaining terms. We combine the vertical advection and residual terms to yield the net moistening between the two as they nearly cancel each other. Each term in Equation 2 is calculated six hourly and in the longitude-latitude domain first before they are composited based on MJO events. All moisture-related quantities on an event-by-event basis are again scaled by the zonal wavelengths of the MJO (Section 2.3).

To diagnose the relationship between the circulation indices and moisture budget terms, we compute the mean column-integrated moisture budget terms over the same regions that were used to calculate U^* and Z^*. A column-integrated quantity X is denoted by a bracket $\langle X \rangle = \frac{1}{g}\int_{p_1}^{p_2} X\, dp$, integrated from 1,000 hPa through 200 hPa. For simplicity, we hereby refer to the moisture budget terms in Equation 2 from left to right as follows: time tendency as $\frac{dq}{dt}$, zonal advection as *uadv*, meridional advection as *vadv*, vertical advection as *wadv*, and the residual (apparent heating) as *resid*. To partially account for the meridional shift in the maxima of column-integrated specific humidity time-tendency $\langle \frac{dq}{dt} \rangle$ east of the MJO, we average across ±15° of latitude from the convective center for the moisture budget terms. Figure 5 depicts the regression coefficients of U^* versus all four column-integrated budget terms above across all MJO events identified as a function of reference longitude. In Figure 5, a negative regression coefficient indicates that the moisture budget term tends to have a higher value (stronger contribution to moistening) for MJO events with easterly wind anomalies ahead of the convective center than events with westerly wind anomalies.

U^* has a consistent negative regression coefficient (at time lag = 0) across all reference longitude ranges with $\langle \frac{dq}{dt} \rangle$ and the column integrated meridional advection $\langle vadv \rangle$. In other words, a positive time tendency in $\langle q' \rangle$ and a positive contribution to that tendency from $\langle vadv \rangle$ is statistically associated with anomalous, MJO-related, low-level easterly flow east of the convective center. Statistical significance of these regressions is noted for $\langle \frac{dq}{dt} \rangle$ at 40–60°E and 60–80°E, while statistical significance is indicated for $\langle vadv \rangle$ at 100–120°E and 120–140°E. The sign of regression coefficients of the column-integrated zonal advection $\langle uadv \rangle$ changes from a statistically significantly negative value over 40–60°E to a statistically significant positive value at 120–140°E, with values close to zero in between. This result indicates that zonal advection does not generally contribute to the moistening eastward of MJO convection and it is not the key mechanism that supports the eastward propagation of the MJO. Instead, the existence of easterly wind anomalies supports MJO propagation through meridional advection of moisture, which agrees with some of the findings of D. Kim et al. (2014) and Feng et al. (2015), which both emphasized the role of meridional moisture advection in determining whether an MJO event propagated across the Maritime Continent. The findings from these two studies suggested that these enhanced easterlies were accompanied by anticyclonic flow associated with convectively suppressed regions leading the active convection (D. Kim et al., 2014) or meridional shear associated with the Kelvin wave itself (Feng et al., 2015; L. Wang et al., 2019). Our results also suggest that stronger Kelvin wave easterlies may be coupled with stronger equatorial Rossby wave-like disturbances that lead to additional moistening via meridional advection. The results also highlight the challenge in isolating the effect of Kelvin waves using an index based on zonal wind alone. We will address this issue by combining zonal wind and geopotential height signal later in this section.

The regression coefficient of U^* onto the column-integrated vertical advection and residual term $\langle wadv + resid \rangle$ remains small and insignificant across all longitude ranges. When $\langle wadv \rangle$ and $\langle resid \rangle$ are considered separately, U^* has a negative, regression coefficient with $\langle resid \rangle$, indicating more moistening from the apparent heating with stronger easterly anomalies. Meanwhile, the regression with $\langle wadv \rangle$ is positive and insignificant across all longitudes. This result appears to be inconsistent with the conclusions by Hsu and Li (2012) and B. Wang et al. (2019), who suggested that the enhanced low-level Kelvin wave easterlies were associated with enhanced boundary layer moisture convergence and subsequent vertical moistening of the lower troposphere ahead of the convection.

To assess the vertical structure of the moisture budget terms, Figure 6 shows their cross-sections averaged over ±10° latitude from the convective center over the longitude range of 100–120°E, as this represents where U^* was most significant in affecting propagation probabilities (Figure 3). Shadings in Figures 6a–6c show the regression coefficients of the budget terms with U^* east of the convective center. Contours show the regression of $\frac{dq}{dt}$ with U^* and stippling indicates its statistical significance. The significance of the budget terms is not shown, but generally yielded similar patterns to the time tendency across all longitudes. Negative coefficients indicate that there is more moistening contributed by the given budget term for events with easterly U^*. Statistically significant, negative coefficients in $\frac{dq}{dt}$ primarily appear in the middle troposphere between 700 and 500 hPa, while negative coefficients in the low-levels occur further ahead of the convective center roughly from 120° theta eastward. The contribution to this low-level tendency is strongly associated with the meridional component (*vadv*), while the sum of *vadv* and the vertical component and residual (*wadv* + *resid*) is the strongest contributor to the middle-troposphere coefficient (consistent with Figure 5). Again, the importance of the meridional component of moisture advection is suggested over the Maritime Continent (D. Kim et al., 2014; Feng et al., 2015), and having a stronger anomalous, low-level easterly ahead of the convective center favors a larger positive $\frac{dq}{dt}$ in both the lower and middle troposphere. This pattern consistently appears across all of the longitude ranges. As shown in Figure 6a, we additionally find a statistically significant drying signal to the west of the convective center in the lower to middle troposphere, potentially indicating some role of moisture asymmetry in driving propagation, as in Hsu and Li (2012) and Wei and Ren (2019). This drying signal warrants further investigation.

We also decompose the meridional advection of specific humidity into its temporally-filtered components to examine what terms contribute the most to the full budget term, and by extension, correlate with the circulation indices, as in D. Kim et al. (2014) and Feng et al. (2015).

$$\left(v\frac{\partial q}{\partial y}\right)' = \left(\overline{v}\frac{\partial q'}{\partial y}\right) + \left(v'\frac{\partial \overline{q}}{\partial y}\right) + \left(v'\frac{\partial q'}{\partial y}\right)' + \left(v''\frac{\partial q''}{\partial y}\right)' \tag{3}$$

Here, the term on the left-hand side represents the meridional advection term from Equation 2, while overbars denote the low-pass (100 days) filtered anomalies, single primes denote the intraseasonal filtered anomalies,

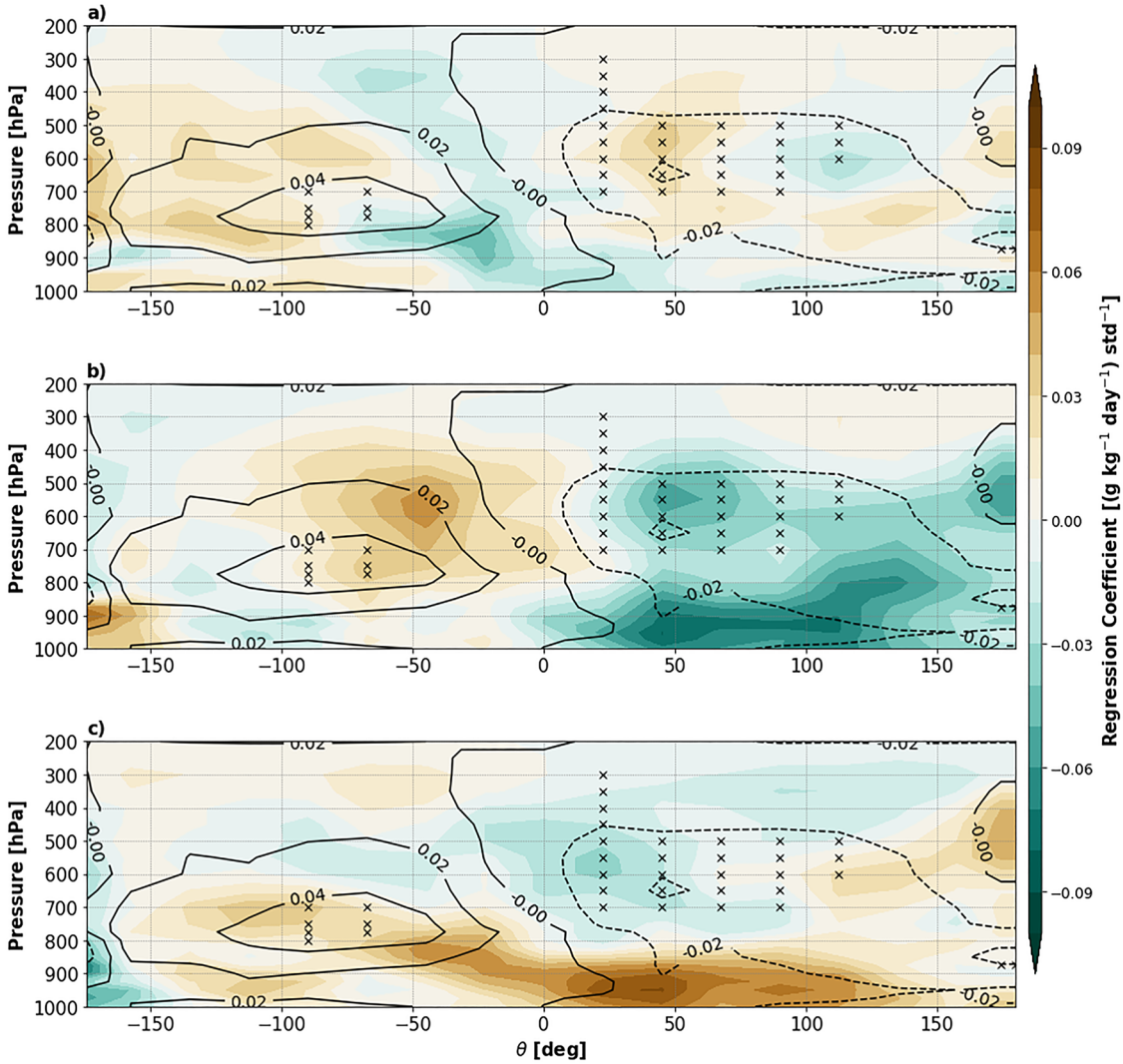

Figure 6. Theta-height cross-section regression coefficients for events centered at 100–120°E between U^* and intraseasonal (a) zonal advection of specific humidity, (b) meridional advection of specific humidity, and (c) vertical advection and the residual (color-shaded, in g kg^{-1} day^{-1} std^{-1}) averaged over ±10° latitude from the convective center. The composite difference of $\frac{dq}{dt}$ is plotted (black contours) and significance at the 95% confidence level is indicated by X-stippling.

and double primes denote the high-pass (20-day) filtered anomalies. Therefore, the terms on the right-hand side represent from left to right; meridional advection of intraseasonal q by the background wind, meridional advection of background q by the intraseasonal wind, meridional advection of intraseasonal q by the intraseasonal wind, and meridional advection of high-frequency q by the high-frequency wind.

Figure 7 shows this decomposition by displaying the regression coefficients of these terms and their sum with U^* at 100–120°E. Here, the advection of background q by the intraseasonal meridional wind is the dominant contributor to the overall budget term, suggesting that MJO-related poleward advection across the mean moisture gradient is most important as suggested by prior studies (D. Kim et al., 2014; Feng et al., 2015). Some contribution from the combination of higher frequency eddies and high frequency variations in q is noted further east in the lower and middle troposphere, along with some low-level negative coefficients from the background wind advecting intraseasonal q.

To understand why easterlies lead to increased moistening via meridional advection, the theta–latitude regression of the intraseasonal 850 hPa horizontal wind onto U^* at 100–120°E is shown in Figure 8, along with the intraseasonal meridional advection budget term. As shown in Figure 7b, the meridional advection term shows negative regressions with U^* across a range of latitudes east of the convective center. Separate tests at 700 and 500 hPa

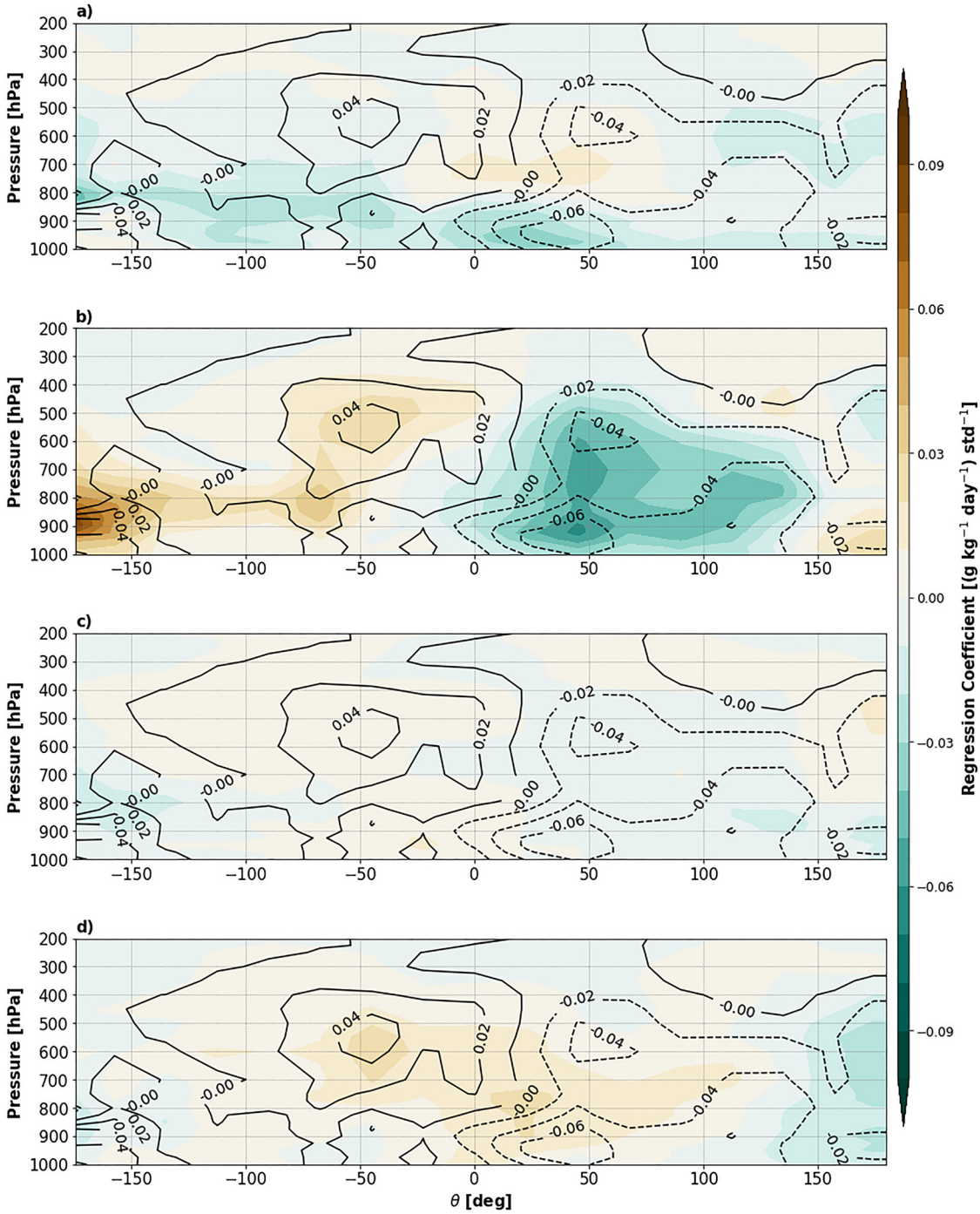

Figure 7. Regression coefficients with U^* at 100–120°E for meridional advection of (a) intraseasonal q by the background wind, (b) background q by the intraseasonal wind, (c) intraseasonal q by the intraseasonal wind, and (d) high-frequency q by the high-frequency wind (color-shaded, in g kg^{-1} day^{-1} std^{-1}). Black contours are the sum of the regression coefficients of all four terms.

revealed similar findings (not shown). The horizontal winds show that equatorial easterlies are associated with stronger poleward meridional winds, which would result in moisture being advected away from the mean background moisture maximum (contours) on the intraseasonal timescale. This result indicates that the poleward moisture advection may be associated with anticyclonic Rossby-wave response to preceding MJO suppressed convection. To further examine the relationship between U^* and the poleward flow associated with the Rossby waves, we generated an index to quantify the strength of Rossby waves. This index (V^*) is formed by finding a

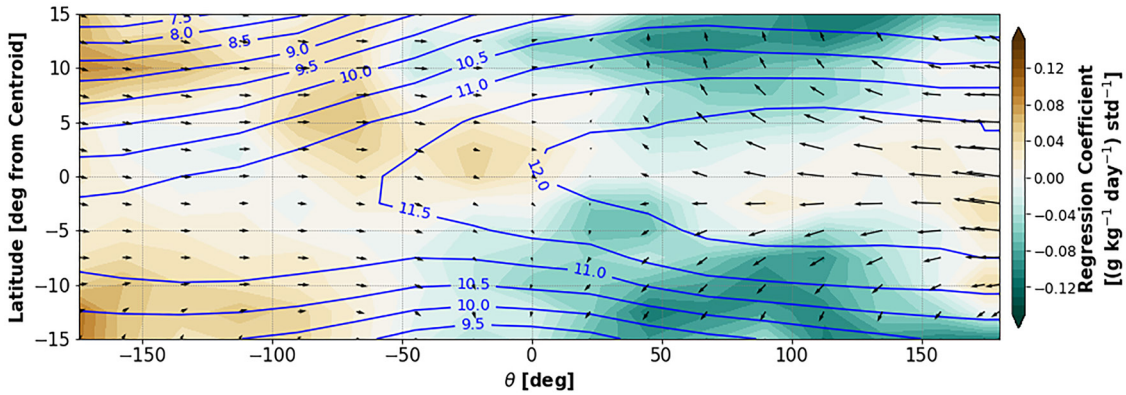

Figure 8. Regression coefficients with U^* at 100–120°E for 850 hPa meridional advection of background specific humidity by the intraseasonal wind (color-shaded, in g kg^{-1} day^{-1} std^{-1}) and horizontal wind (vectors, in m s^{-1}). The negative of the regression coefficient of wind is plotted to show the effect as U^* becomes more negative. Blue contours represent the mean 850 hPa background specific humidity for all cases used to compute the regression.

difference between the meridional wind at north and south relative to the convective center, averaged between zonal phase of 33.75 and 101.25°. We found a significant negative correlation between U^* and V^* (not shown), confirming the strong coupling between easterly wind and poleward flow that leads to the meridional advection of moisture. The poleward meridional winds may also be associated with a westward propagating intraseasonal mode (WPIM) identified in Gonzalez and Jiang (2019). Interactions between the WPIM and MJO may therefore influence MJO propagation when both of these modes are active. Coupling between the Kelvin circulation east of active convection and these antecedent features is therefore potentially important for supporting eastward propagation.

The aforementioned coupling between the easterly wind and poleward flow makes it difficult to conclude if the existence of easterlies support MJO propagation due to the presence of Kelvin or Rossby waves. In addition to the easterly wind, Section 3 showed that the presence of negative geopotential height leads to higher probability of MJO eastward propagation. Therefore, to understand what process might contribute to this enhanced propagation, Figure 9 depicts the regressions of the column-integrated budget terms with Z^*, given an easterly wind anomaly ahead of the convection. In other words, these regressions are assessed when a Kelvin wave signal is evident in both U^* and Z^* versus when it is only present in U^*, which could come from either Kelvin or Rossby wave. The regression with $\langle \frac{dq}{dt} \rangle$ remains weakly negative across the full range of longitude ranges, but weakens over 120–140°E, indicating at least a modest tendency for events with negative geopotential height east of the convective center to have more moistening in the same region. There is a flip in the signs of the regressions associated with $\langle vadv \rangle$ and $\langle wadv + resid \rangle$, with regressions near zero around 80–100°E. The weak negative regression with $\langle vadv \rangle$ over the Indian Ocean indicates its contribution to greater moistening when there are negative geopotential height anomalies. However, its regression sign changes to positive over the western Pacific, which indicates

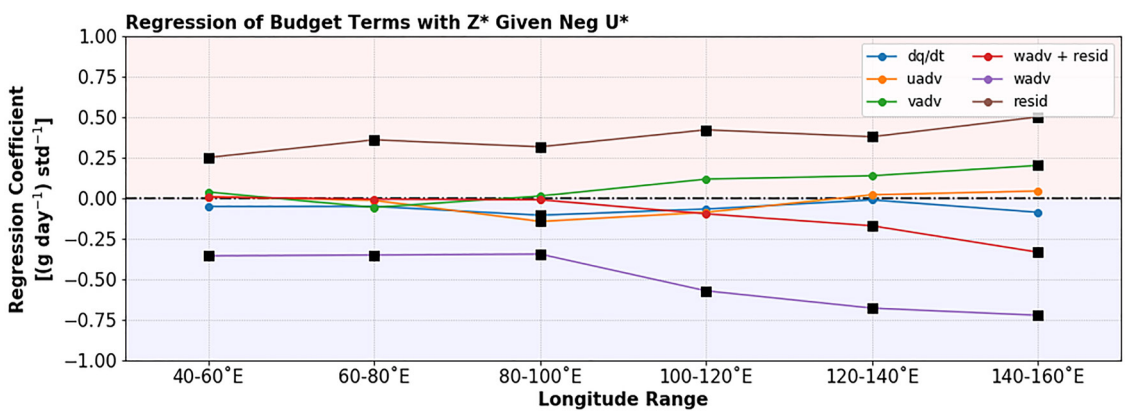

Figure 9. As in Figure 5, but instead for cases with negative U^* and for the regression with Z^* states east of the transition.

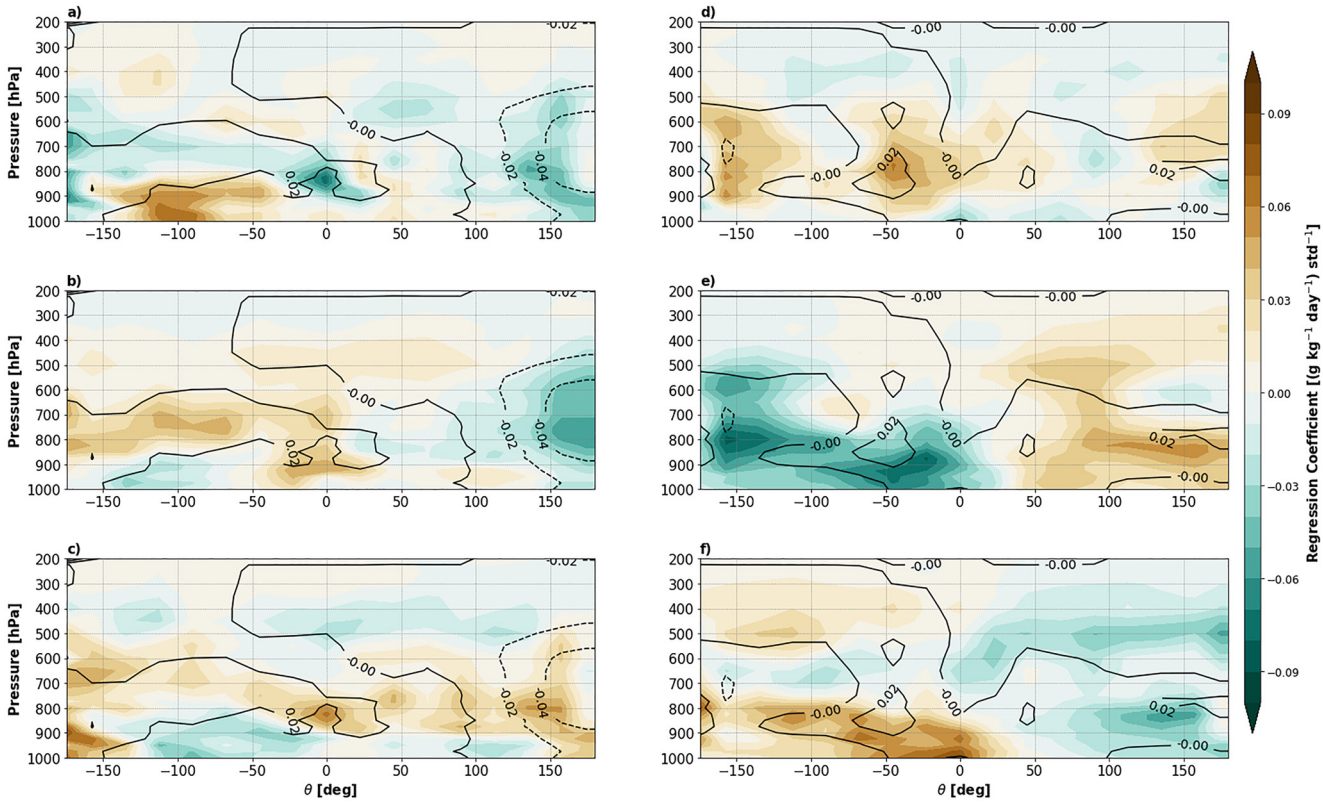

Figure 10. As in Figure 6, but for the regressions of budget terms with Z^* when U^* is easterly for events centered at (a–c) 40–60°E and (d–f) 120–140°E.

that the events with negative geopotential height anomalies would tend to have less moistening or drying from $\langle vadv \rangle$ over this region. This may be a result of detours in the track of the MJO away from the mean moisture maximum as it propagates further east, where equatorward flow may result from a negative geopotential height anomaly. The reverse is true for $\langle wadv + resid \rangle$. As in Figure 5, we also compute the regressions with $\langle wadv \rangle$ and $\langle resid \rangle$ separately. As with using U^* only, $\langle resid \rangle$ has a positive, significant regression with Z^* across all longitudes, indicating more drying takes place with lower pressure east of the convection. However, unlike for U^* only, $\langle wadv \rangle$ has a negative and significant regression across all longitudes with Z^*. Therefore, the presence of negative Z^* in addition to easterly U^* encourages more boundary layer convergence and vertical moistening than easterly U^* alone, despite the drying from the apparent heating term, which is consistent with the findings of Yang and Wang (2019). These results suggest that a Kelvin wave signal leads to a stronger contribution to moistening through $\langle wadv + resid \rangle$, particularly over the western Pacific. Similar results were found when the budget terms were integrated for the lower-tropospheric levels (1,000–700 hPa) only (not shown).

The negative regressions of Z^* with $\langle vadv \rangle$ over 60–80°E and U^* with $\langle vadv \rangle$ over 80–100°E, 100–120°E and 120–140°E suggest some role of the meridional advection in assisting propagation, as these are the reference longitudes where negative Z^* and easterly U^* have the most significance in the probability of propagation analysis (Figures 3 and 4). Rather strong, statistically significant negative regressions between Z^* and $\langle wadv + resid \rangle$ east of 100°E suggest that the boundary layer moisture convergence and associated vertical advection may be related to regions of low pressure within the Kelvin circulation over the Maritime Continent and eastward (B. Wang et al., 2019; Wang & Rui, 1990), but the strength of the low-level easterlies within the Kelvin region alone is not particularly associated with the anomalous vertical moistening of the low-levels (Figure 5).

Figures 10a–10c shows the same as Figure 6, except showing the regression between budget terms and Z^* when U^* was easterly for the reference longitude range of 40–60°E, as this represents where Z^* was most significant in affecting the propagation probabilities (Figure 4). We also include the budget terms regressed at 120–140°E in Figures 10d–10f. While the regressions of Z^* with $\frac{dq}{dt}$ do not reach the 95% confidence level, a separate test using the 90% confidence level (not shown) showed some statistically significant negative regressions in the

middle-levels ahead of the convective center at 40–60°E. The negative regression coefficients of moisture tendency (more moistening with lower Z^*) ahead of the convective center at 40–60°E is again primarily related to the horizontal components of moisture advection, particularly *vadv*, except near 500 hPa and above, where a comparatively small negative regression coefficient in *wadv* + *resid* exists. Figure 10f suggests a negative regression between the *wadv* + *resid* term and Z^* as in Figure 9, therefore indicating that the importance of the *wadv* + *resid* term when using Z^* as the circulation index seems to rise over the Maritime Continent and West Pacific. However, as Figure 4 suggested, the positive differences in propagation probabilities are not as large over these regions, nor are they as consistently significant as further west. In addition, the time tendency itself actually has a positive regression coefficient east of the active convection in Figures 10d–10f, indicating that there is more drying as Z^* becomes more negative over these regions. When *wadv* and *resid* are separated, there is positive contribution to moistening from *wadv* in the lower and middle troposphere, but the residual tends to cancel it out in the lower troposphere (L. Wang & Li, 2020). For the middle troposphere, some moistening remained when considering *wadv*, but the regression was not as strong as with *vadv*. These results suggest that the Kelvin wave acts to enhance boundary layer convergence over the western Pacific, but its moistening is canceled out by other processes and does not lead to greatly increased probability of propagation as shown in Figure 4. Furthermore, relationships between the circulation indices and the upward-directed surface latent heat flux (not shown) were weak and did not display significance across all longitude ranges, indicating that the state of the circulation had little effect on the surface latent heat flux. While L. Wang and Li (2020) indicated moistening occurred due to Q_2 when the MJO is centered at 120°E due to enhanced easterlies over the Pacific, our results suggest that the strength of these easterlies does not have a strong relationship with the latent heat flux.

Therefore, while some influence of the *wadv* term is suggested near/over the Maritime Continent, as implied by studies such as Hsu and Li (2012) and B. Wang et al. (2019), such an influence is not consistent across all longitudes given the opposing contribution from the *resid* term. The existence of Kelvin wave signal, identified by the presence of both easterly winds and negative geopotential height, enhances MJO eastward propagation primarily over the Indian Ocean (Figure 4), where it is associated with enhanced moistening via meridional advection (Figure 9). Therefore, the effect of the Kelvin wave on MJO propagation may still be indirect due to its strong coupling with the Rossby wave that tends to strengthen with Kelvin wave signal. Despite this, having lower pressures (negative Z^*) east of MJO convection does appear to encourage more vertical moistening from boundary layer convergence (Figure 9), especially once the MJO moves over the Maritime Continent, and therefore the role of *wadv* should not be fully discounted.

5. Conclusion and Discussion

Eastward propagation of the MJO, especially over the Maritime Continent, remains an issue in operational and climate models. To improve our understanding of MJO propagation, this study assessed the relationship between MJO circulation and its propagation over the Maritime Continent. We developed a new method to quantify MJO circulation independent of its zonal scale over differing regions. Prior studies suggest that a Kelvin circulation leading MJO convection can support MJO propagation through horizontal advection (Adames & Kim, 2016; Adames & Wallace, 2015; Feng et al., 2015) and frictional boundary convergence (B. Wang et al., 2016, 2019; Hsu & Li, 2012; Wei & Ren, 2019). Therefore, a probability analysis was conducted to test the impact of both the lower-tropospheric zonal wind and geopotential height anomalies within the Kelvin circulation on MJO propagation. An intraseasonal moisture budget analysis was conducted to link the results found in the probability analysis with physical processes known to affect the evolution of the MJO (A. H. Sobel et al., 2001; Adames & Kim, 2016; A. Sobel & Maloney, 2012; Chen & Wang, 2019).

In agreement with prior studies, we found that the existence of equatorial easterlies east of MJO convection increases the chance of its propagation, especially around the Maritime Continent (Figure 3). A new finding of this study is that the presence of negative geopotential height east of MJO convection over the Indian Ocean further increases the chances of eastward propagation (Figure 4). Probabilities of propagation are highest when anomalous easterlies and negative geopotential height are both present east of MJO convection (a Kelvin circulation, Figure 4a). These results indicate that zonal wind and geopotential height signals consistent with Kelvin waves play a role in supporting MJO eastward propagation. However, the effect of the Kelvin wave on MJO eastward propagation may be indirect through the strong coupling between Kelvin and Rossby wave circulation.

A moisture budget analysis indicates that the MJO with a strong Kelvin wave signal tend to propagate across the Maritime Continent through enhanced environmental moistening stemming from meridional advection. The strongest contributor to the overall meridional advection is the meridional advection of background specific humidity by the intraseasonal wind. Stronger Kelvin wave circulation east of MJO convection is coupled with anticyclonic equatorial Rossby circulations associated with a suppressed convective phase and dry signal leading the active convection or a separate westward propagating intraseasonal mode (DeMott et al., 2018; D. Kim et al., 2014; Gonzalez & Jiang, 2019). Therefore, although Kelvin waves do not produce strong meridional winds, the associated equatorial Rossby waves could potentially lead to moistening through meridional advection and support MJO eastward propagation.

The importance of individual moisture budget terms also changes depending on the region that is assessed. Stronger negative geopotential height collocated with the Kelvin circulation east of the convective center leads to stronger moistening through vertical advection. This result may be partially related to meridional shifting of the active convection and circulation over these longitudes (D. Kim et al., 2017) and maturation of the circulation response (Adames & Wallace, 2015; Kiladis et al., 2005), which warrants further investigation. Our results suggests that previous studies such as B. Wang et al. (2019) that linked further propagation to primarily boundary layer moisture convergence and subsequent vertical moistening of the lower troposphere based on a "stronger Kelvin response" may only be applicable over a limited region. While vertical advection from boundary layer convergence contributes—especially when considering geopotential height anomalies east of the convection—through the lenses of our coordinate transformation methodology, it does not appear to be the primary factor in encouraging MJO propagation. In contrast, moistening via the meridional advection is shown to play an important role in enhancing MJO propagation throughout all longitudes.

This study focused on understanding the moistening processes associated with the MJO under the "moisture mode" framework (A. H. Sobel et al., 2001), but we acknowledge that dry wave dynamics may play an additional role. We additionally acknowledge that our method and choice of data do not resolve smaller scale features that may be an important aspect in impacting moistening processes, particularly within the boundary layer. Such smaller scale features may therefore suggest a stronger relationship between boundary layer convergence and subsequent vertical moistening and MJO propagation than indicated in this study.

Our study provided further insights into how the Kelvin-Rossby wave circulation relates to MJO propagation. The new method to quantify these waves can be applied to GCMs and operational models, which would help assess model performance and MJO prediction skill. The circulation indices outlined here cannot be directly implemented operationally given the filtering performed in order to yield them, but some adjustments can be made to be applied operationally. The lack of closure in the moisture budget in ERA-Interim (Adames & Wallace, 2015; Kiranmayi & Maloney, 2011) also presents a caveat to the analysis, as does the derived nature of the vertical velocity fields, although vertical velocity has been shown to be well represented in ERA-Interim (Adames & Wallace, 2014). Further analysis and improvement of diagnostic indices using both observations, other reanalyzes, and modeling will help further improve our understanding of MJO propagation.

Data Availability Statement

Datasets used in this manuscript are publicly available. ERA-Interim data (Dee et al., 2011) were obtained from the ECMWF data server and can be accessed at https://www.ecmwf.int/en/forecasts/datasets/reanalysis-datasets/era-interim. NOAA OLR data (Liebmann & Smith, 1996) were obtained from the NOAA PSD data server and can be accessed at https://psl.noaa.gov/data/gridded/data.interp_OLR.html.

Acknowledgments
The authors would like to thank Brandon Wolding for helpful comments and correspondence during the development of this manuscript and five anonymous reviewers who provided additional comments and constructive criticisms that improved the manuscript significantly from its original version. This research was supported by funding from the NOAA Climate Office through Grant NA16OA4320115.

References

Adames, Á. F., & Kim, D. (2016). The MJO as a dispersive, convectively coupled moisture wave: Theory and observations. *Journal of the Atmospheric Sciences*, *73*(3), 913–941. https://doi.org/10.1175/JAS-D-15-0170.1

Adames, Á. F., & Wallace, J. M. (2014). Three-dimensional structure and evolution of the MJO and its relation to the mean flow. *Journal of the Atmospheric Sciences*, *71*(6), 2007–2026. https://doi.org/10.1175/JAS-D-13-0254.1

Adames, Á. F., & Wallace, J. M. (2015). Three-dimensional structure and evolution of the moisture field in the MJO. *Journal of the Atmospheric Sciences*, *72*(10), 3733–3754. https://doi.org/10.1175/JAS-D-15-0003.1

Ahn, M. S., Kim, D., Ham, Y. G., & Park, S. (2020). Role of maritime continent land convection on the mean state and MJO propagation. *Journal of Climate*, *33*(5), 1659–1675. https://doi.org/10.1175/JCLI-D-19-0342.1

Barrett, B. S., & Leslie, L. M. (2009). Links between tropical cyclone activity and Madden-Julian Oscillation phase in the North Atlantic and Northeast Pacific basins. *Monthly Weather Review*, *137*(2), 727–744. https://doi.org/10.1175/2008MWR2602.1

Bessafi, M., & Wheeler, M. C. (2006). Modulation of South Indian Ocean tropical cyclones by the Madden-Julian Oscillation and convectively coupled equatorial waves. *Monthly Weather Review*, *134*(2), 638–656. https://doi.org/10.1175/MWR3087.1

Chen, G., & Wang, B. (2018). Effects of enhanced front walker cell on the eastward propagation of the MJO. *Journal of Climate*, *31*(19), 7719–7738. https://doi.org/10.1175/JCLI-D-17-0383.1

Chen, G., & Wang, B. (2019). Dynamic moisture mode versus moisture mode in MJO dynamics: Importance of the wave feedback and boundary layer convergence feedback. *Climate Dynamics*, *52*(9–10), 5127–5143. https://doi.org/10.1007/s00382-018-4433-7

Chen, G., & Wang, B. (2020). Circulation factors determining the propagation speed of the Madden–Julian Oscillation. *Journal of Climate*, *33*(8), 3367–3380. https://doi.org/10.1175/jcli-d-19-0661.1

Dee, D. P., Uppala, S. M., Simmons, A. J., Berrisford, P., Poli, P., Kobayashi, S., et al. (2011). The ERA-Interim reanalysis: Configuration and performance of the data assimilation system [Dataset]. Quarterly Journal of the Royal Meteorological Society, *137*(656), 553–597. Retrieved from https://rmets.onlinelibrary.wiley.com/doi/abs/10.1002/qj.828

DeMott, C. A., Wolding, B. O., Maloney, E. D., & Randall, D. A. (2018). Atmospheric Mechanisms for MJO decay over the maritime continent. *Journal of Geophysical Research: Atmospheres*, *123*(10), 5188–5204. https://doi.org/10.1029/2017JD026979

Dias, J., Sakaeda, N., Kiladis, G. N., & Kikuchi, K. (2017). Influences of the MJO on the space-time organization of tropical convection. *Journal of Geophysical Research*, *122*(15), 8012–8032. https://doi.org/10.1002/2017JD026526

Feng, J., Li, T., & Zhu, W. (2015). Propagating and nonpropagating MJO events over maritime continent. *Journal of Climate*, *28*(21), 8430–8449. https://doi.org/10.1175/JCLI-D-15-0085.1

Ferranti, L., Palmer, T. N., Molteni, F., & Klinker, E. (1990). Tropical-extratropical interaction associated with the 30-60 day oscillation and its impact on medium and extended range prediction. *Journal of the Atmospheric Sciences*, *47*(18), 2177–2199. https://doi.org/10.1175/1520-0469(1990)047<2177:teiawt>2.0.co;2

Fu, J. X., Lee, J. Y., Wang, B., Wang, W., & Vitart, F. (2013). Intraseasonal forecasting of the Asian summer monsoon in four operational and research models. *Journal of Climate*, *26*(12), 4186–4203. https://doi.org/10.1175/JCLI-D-12-00252.1

Gill, A. E. (1980). Some simple solutions for heat-induced tropical circulation. *Quarterly Journal of the Royal Meteorological Society*, *106*(449), 447–462. https://doi.org/10.1002/qj.49710644905

Gonzalez, A. O., & Jiang, X. (2017). Winter mean lower tropospheric moisture over the maritime continent as a climate model diagnostic metric for the propagation of the Madden-Julian Oscillation. *Geophysical Research Letters*, *44*(5), 2588–2596. https://doi.org/10.1002/2016GL072430

Gonzalez, A. O., & Jiang, X. (2019). Distinct propagation characteristics of intraseasonal variability over the tropical West Pacific. *Journal of Geophysical Research: Atmospheres*, *124*(10), 5332–5351. https://doi.org/10.1029/2018JD029884

Gottschalck, J., Roundy, P. E., Schreck, C. J., Vintzileos, A., & Zhang, C. (2013). Large-scale atmospheric and oceanic conditions during the 2011–12 DYNAMO field campaign. *Monthly Weather Review*, *141*(12), 4173–4196. https://doi.org/10.1175/MWR-D-13-00022.1

Hamill, T. M., & Kiladis, G. N. (2014). Skill of the MJO and Northern Hemisphere blocking in GEFS medium-range reforecasts. *Monthly Weather Review*, *142*(2), 868–885. https://doi.org/10.1175/MWR-D-13-00199.1

Henderson, S. A., Maloney, E. D., & Barnes, E. A. (2016). The influence of the Madden-Julian Oscillation on Northern Hemisphere winter blocking. *Journal of Climate*, *29*(12), 4597–4616. https://doi.org/10.1175/JCLI-D-15-0502.1

Hendon, H. H., & Salby, M. L. (1994). The life cycle of the Madden–Julian Oscillation. *Journal of the Atmospheric Sciences*, *51*(15), 2225–2237. https://doi.org/10.1175/1520-0469(1994)051⟨2225:tlcotm⟩2.0.co;2

Hsu, P. C., & Li, T. (2012). Role of the boundary layer moisture asymmetry in causing the eastward propagation of the Madden-Julian Oscillation. *Journal of Climate*, *25*(14), 4914–4931. https://doi.org/10.1175/JCLI-D-11-00310.1

Jiang, X., Adames, Á. F., Kim, D., Maloney, E. D., Lin, H., Kim, H., et al. (2020). Fifty years of research on the Madden-Julian Oscillation: Recent progress, challenges, and perspectives. *Journal of Geophysical Research: Atmospheres*, *125*(17). https://doi.org/10.1029/2019JD030911

Jiang, X., Waliser, D. E., Xavier, P. K., Petch, J., Klingaman, N. P., Woolnough, S. J., et al. (2015). Vertical structure and physical processes of the Madden-Julian Oscillation: Exploring key model physics in climate simulations. *Journal of Geophysical Research*, *120*(10), 4718–4748. https://doi.org/10.1002/2014JD022375

Johnson, R. H., & Ciesielski, P. E. (2017). Multiscale variability of the atmospheric boundary layer during DYNAMO. *Journal of the Atmospheric Sciences*, *74*(12), 4003–4021. https://doi.org/10.1175/JAS-D-17-0182.1

Kemball-Cook, S. R., & Weare, B. C. (2001). The onset of convection in the Madden-Julian Oscillation. *Journal of Climate*, *14*(5), 780–793. https://doi.org/10.1175/1520-0442(2001)014<0780:toocit>2.0.co;2

Kerns, B. W., & Chen, S. S. (2016). Large-scale precipitation tracking and the MJO over the Maritime Continent and Indo-Pacific warm pool. *Journal of Geophysical Research*, *121*(15), 8755–8776. https://doi.org/10.1002/2015JD024661

Kiladis, G. N., Straub, K. H., & Haertel, P. T. (2005). Zonal and vertical structure of the Madden-Julian Oscillation. https://doi.org/10.1175/JAS3520.1

Kim, D., Kim, H., & Lee, M. I. (2017). Why does the MJO detour the maritime continent during austral summer? *Geophysical Research Letters*, *44*(5), 2579–2587. https://doi.org/10.1002/2017GL072643

Kim, D., Kug, J. S., & Sobel, A. H. (2014). Propagating versus nonpropagating Madden-Julian Oscillation events. *Journal of Climate*, *27*(1), 111–125. https://doi.org/10.1175/JCLI-D-13-00084.1

Kim, D., Sperber, K., Stern, W., Waliser, D., Kang, I. S., Maloney, E., et al. (2009). Application of MJO simulation diagnostics to climate models. *Journal of Climate*, *22*(23), 6413–6436. https://doi.org/10.1175/2009JCLI3063.1

Kim, H. M., Kim, D., Vitart, F., Toma, V. E., Kug, J. S., & Webster, P. J. (2016). MJO propagation across the maritime continent in the ECMWF ensemble prediction system. *Journal of Climate*, *29*(11), 3973–3988. https://doi.org/10.1175/JCLI-D-15-0862.1

Kim, H. M., Webster, P. J., Toma, V. E., & Kim, D. (2014). Predictability and prediction skill of the MJO in two operational forecasting systems. *Journal of Climate*, *27*(14), 5364–5378. https://doi.org/10.1175/JCLI-D-13-00480.1

Kiranmayi, L., & Maloney, E. D. (2011). Intraseasonal moist static energy budget in reanalysis data. *Journal of Geophysical Research*, *116*(D21). https://doi.org/10.1029/2011JD016031

Klotzbach, P. J. (2010). On the Madden-Julian Oscillation-Atlantic hurricane relationship. *Journal of Climate*, *23*(2), 282–293. https://doi.org/10.1175/2009JCLI2978.1

Lawrence, D. M., & Webster, P. J. (2002). The boreal summer intraseasonal oscillation: Relationship between northward and eastward movement of convection. *Journal of the Atmospheric Sciences*, *59*(9), 1593–1606. https://doi.org/10.1175/1520-0469(2002)059<1593:tbsior>2.0.co;2

Lee, J. Y., Wang, B., Wheeler, M. C., Fu, X., Waliser, D. E., & Kang, I. S. (2013). Real-time multivariate indices for the boreal summer intraseasonal oscillation over the Asian summer monsoon region. *Climate Dynamics*, *40*(1–2), 493–509. https://doi.org/10.1007/s00382-012-1544-4

Liebmann, B., & Smith, A. (1996). Outgoing long-wave radiation [Dataset]. Bulletin of the American Meteorological Society, *77*(6), 1275–1277. Retrieved from https://www.jstor.org/stable/26233278

Ling, J., Zhang, C., Joyce, R., ping Xie, P., & Chen, G. (2019). Possible role of the diurnal cycle in land convection in the barrier effect on the MJO by the maritime continent. *Geophysical Research Letters*, *46*(5), 3001–3011. https://doi.org/10.1029/2019GL081962

Madden, R. A., & Julian, P. R. (1971). Detection of a 40–50 day oscillation in the zonal wind in the tropical Pacific. *Journal of the Atmospheric Sciences*, *28*(5), 702–708. https://doi.org/10.1175/1520-0469(1971)028⟨0702:doadoi⟩2.0.co

Madden, R. A., & Julian, P. R. (1994). Observations of the 40-50-day tropical oscillation—A review. *Monthly Weather Review*, *122*(5), 814–837. https://doi.org/10.1175/1520-0493(1994)122<0814:ootdto>2.0.co;2

Maloney, E. D., & Hartmann, D. L. (2000). Modulation of hurricane activity in the Gulf of Mexico by the Madden- Julian oscillation. *Science*, *287*(5460), 2002–2004. https://doi.org/10.1126/science.287.5460.2002

Matsuno, T. (1966). Quasi-geostrophic motions in the equatorial area. *Journal of the Meteorological Society of Japan. Series II*, *44*(1), 25–43. https://doi.org/10.2151/jmsj1965.44.1_25

Pai, D. S., Bhate, J., Sreejith, O. P., & Hatwar, H. R. (2011). Impact of MJO on the intraseasonal variation of summer monsoon rainfall over India. *Climate Dynamics*, *36*(1–2), 41–55. https://doi.org/10.1007/s00382-009-0634-4

Riley, E. M., Mapes, B. E., & Tulich, S. N. (2011). Clouds associated with the Madden-Julian Oscillation: A new perspective from Cloudsat. *Journal of the Atmospheric Sciences*, *68*(12), 3032–3051. https://doi.org/10.1175/JAS-D-11-030.1

Sakaeda, N., Kiladis, G., & Dias, J. (2020). The diurnal cycle of rainfall and the convectively coupled equatorial waves over the maritime continent. *Journal of Climate*, *33*(8), 3307–3331. https://doi.org/10.1175/jcli-d-19-0043.1

Sobel, A., & Maloney, E. (2012). An idealized semi-empirical framework for modeling the Madden-Julian Oscillation. *Journal of the Atmospheric Sciences*, *69*(5), 1691–1705. https://doi.org/10.1175/JAS-D-11-0118.1

Sobel, A. H., Nilsson, J., & Polvani, L. M. (2001). The weak temperature gradient approximation and balanced tropical moisture waves. *Journal of the Atmospheric Sciences*, *58*(23), 3650–3665. https://doi.org/10.1175/1520-0469(2001)058<3650:twtgaa>2.0.co;2

Vitart, F., & Molteni, F. (2010). Simulation of the Madden-Julian Oscillation and its teleconnections in the ECMWF forecast system. *Quarterly Journal of the Royal Meteorological Society*, *136*(649), 842–855. https://doi.org/10.1002/qj.623

Wang, B., Chen, G., & Liu, F. (2019). Diversity of the Madden-Julian Oscillation. *Science Advances*, *5*(7). https://doi.org/10.1126/sciadv.aax0220

Wang, B., & Lee, S. S. (2017). MJO propagation shaped by zonal asymmetric structures: Results from 24 GCM simulations. *Journal of Climate*, *30*(19), 7933–7952. https://doi.org/10.1175/JCLI-D-16-0873.1

Wang, B., Liu, F., & Chen, G. (2016). A trio-interaction theory for Madden–Julian Oscillation. https://doi.org/10.1186/s40562-016-0066-z

Wang, B., & Rui, H. (1990). Dynamics of the coupled moist Kelvin-Rossby wave on an equatorial β-plane. *Journal of the Atmospheric Sciences*, *47*(4), 397–413. https://doi.org/10.1175/1520-0469(1990)047⟨0397:dotcmk⟩2.0.co

Wang, B., & Xie, X. (1997). A Model for the boreal summer intraseasonal oscillation. *Journal of the Atmospheric Sciences*, *54*(1), 72–86. https://doi.org/10.1175/1520-0469(1997)054<0072:amftbs>2.0.co;2

Wang, L., & Li, T. (2020). Reexamining the MJO moisture mode theories with normalized phase evolutions. *Journal of Climate*, *33*(19), 8523–8536. https://doi.org/10.1175/JCLI-D-20-0202.1

Wang, L., Li, T., & Chen, L. (2019b). Modulation of the Madden–Julian oscillation on the energetics of wintertime synoptic-scale disturbances. *Climate Dynamics*, *52*(7–8), 4861–4871. https://doi.org/10.1007/s00382-018-4447-1

Wang, L., Li, T., & Nasuno, T. (2018). Impact of Rossby and Kelvin wave components on MJO eastward propagation. *Journal of Climate*, *31*(17), 6913–6931. https://doi.org/10.1175/JCLI-D-17-0749.1

Weaver, S. J., Wang, W., Chen, M., & Kumar, A. (2011). Representation of MJO variability in the NCEP climate forecast system. *Journal of Climate*, *24*(17), 4676–4694. https://doi.org/10.1175/2011JCLI4188.1

Wei, Y., & Ren, H. L. (2019). Modulation of ENSO on fast and slow MJO modes during boreal winter. *Journal of Climate*, *32*(21), 7483–7506. https://doi.org/10.1175/JCLI-D-19-0013.1

Wheeler, M., & Kiladis, G. N. (1999). Convectively coupled equatorial Waves: Analysis of Clouds and temperature in the wavenumber-frequency domain. *Journal of the Atmospheric Sciences*, *56*(3), 374–399. https://doi.org/10.1175/1520-0469(1999)056<0374:ccewao>2.0.co;2

Wheeler, M. C., & Hendon, H. H. (2004). An all-season real-time multivariate MJO index: Development of an index for monitoring and prediction. *Monthly Weather Review*, *132*(8), 1917–1932. https://doi.org/10.1175/1520-0493(2004)132<1917:aarmmi>2.0.co;2

Yanai, M., Esbensen, S., & Chu, J.-H. (1973). Determination of bulk properties of tropical cloud clusters from large-scale heat and moisture budgets. *Journal of the Atmospheric Sciences*, *30*(4), 611–627. https://doi.org/10.1175/1520-0469(1973)030<0611:dobpot>2.0.co;2

Yanai, M., & Johnson, R. H. (1993). Impacts of Cumulus convection on thermodynamic fields. *The representation of cumulus convection in numerical models*, 39–62. https://doi.org/10.1007/978-1-935704-13-3_4

Yang, Y. M., & Wang, B. (2019). Improving MJO simulation by enhancing the interaction between boundary layer convergence and lower tropospheric heating. *Climate Dynamics*, *52*(7–8), 4671–4693. https://doi.org/10.1007/s00382-018-4407-9

Yoo, C., Lee, S., & Feldstein, S. B. (2012). Mechanisms of Arctic surface air temperature change in response to the Madden-Julian Oscillation. *Journal of Climate*, *25*(17), 5777–5790. https://doi.org/10.1175/JCLI-D-11-00566.1

Zhang, C. (2005). Madden-Julian Oscillation. https://doi.org/10.1029/2004RG000158

Zhang, C., & Ling, J. (2017). Barrier effect of the Indo-Pacific maritime continent on the MJO: Perspectives from tracking MJO precipitation. *Journal of Climate*, *30*(9), 3439–3459. https://doi.org/10.1175/JCLI-D-16-0614.1